

A Revised Underwater Image Formation Model

Derya Akkaynak Tali Treibitz

University of Haifa

derya.akkaynak@gmail.com, ttreibitz@univ.haifa.ac.il

Abstract

The current underwater image formation model descends from atmospheric dehazing equations where attenuation is a weak function of wavelength. We recently showed that this model introduces significant errors and dependencies in the estimation of the direct transmission signal because underwater, light attenuates in a wavelength-dependent manner. Here, we show that the backscattered signal derived from the current model also suffers from dependencies that were previously unaccounted for. In doing so, we use oceanographic measurements to derive the physically valid space of backscatter, and further show that the wideband coefficients that govern backscatter are different than those that govern direct transmission, even though the current model treats them to be the same. We propose a revised equation for underwater image formation that takes these differences into account, and validate it through in situ experiments underwater. This revised model might explain frequent instabilities of current underwater color reconstruction models, and calls for the development of new methods.

1. Introduction

Researchers aiming to color correct underwater images are frequently faced with unstable results: available methods are either not robust, are too sensitive, or only work for short object ranges. This is usually explained by the challenge in the correction, e.g., images having low SNR, severe distortions and loss of color, etc. Here we suggest that there is a more fundamental reason to these instabilities than merely “low quality images”, and show that they stem from using an inaccurate image formation model.

Current underwater color correction methods [5, 8, 9, 12, 13, 26, 27, 31, 36, 40] rely on a commonly used image formation model first derived for haze [3, 4, 14, 17, 39]. However, light propagation in the ocean differs from that in the atmosphere in major ways, which renders this model inadequate when applied to underwater images.

In pure air, attenuation (sum of absorption and scattering) is only due to gas molecules and is an inverse function

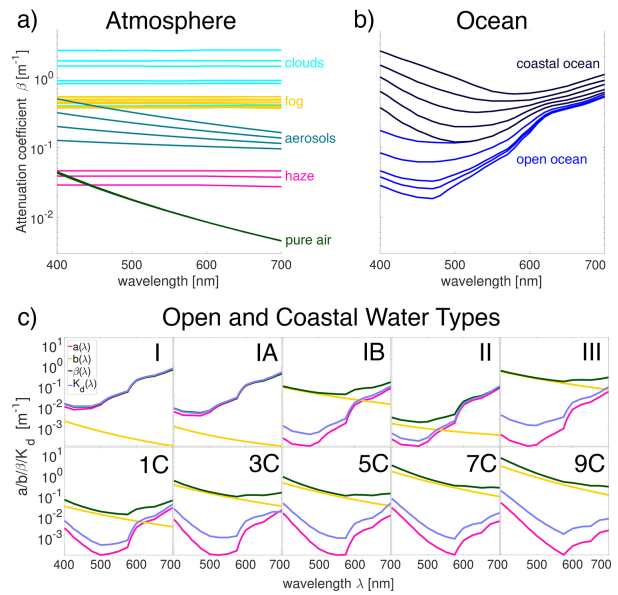


Figure 1. **a)** On the surface of the earth where most photographs are taken, air is mixed with aerosols which increase inscatter, making attenuation independent of wavelength λ . Cloud, fog, and haze coefficients are *in situ* measurements [11]; pure air and aerosol are theoretical values [32]. **b)** In the ocean, attenuation is a strong function of wavelength. **c)** Oceanographer Nils G. Jerlov [21] defined 5 open (I-III) and 5 coastal ocean (1-9C) classes based on the diffuse downwelling attenuation coefficients K_d he measured globally. Here we show coefficients of beam absorption a , scattering b , and β , and K_d for Jerlov’s water types [38]. In contrast to the atmosphere, absorption in the ocean is generally not negligible compared to scattering [22]; e.g., types I (open Pacific), IA (eastern Mediterranean), IB (open Atlantic) are absorption dominated.

of the fourth power of wavelength [24, 32, 25] (Fig. 1a). Near the surface of the earth, however, air is mixed with solid and liquid particles (aerosols) that create the states we call clouds, dust, haze, smoke, smog, mist, fog and vog (fog from volcanic ash). In the presence of aerosols, whose mean diameters can be up to ten times larger than the incident light wavelength, multiple scattering effects become significant and wavelength dependency decreases [32]. In haze and fog, scattering becomes non-selective and attenuation

in the visible part of the electromagnetic spectrum becomes practically independent of wavelength [17, 29, 30, 32] (Fig. 1a).

In contrast to the atmosphere, natural bodies of water exhibit extreme differences in their optical properties (Fig. 1b). Some lakes are as clear as distilled water [15], some are pink [16], and others change color several times a year transitioning between white, blue, green, red, brown, and black [34]. In the ocean, coastal harbors are often brown and murky while offshore waters are blue and clear [1, 21]. Thus, a major difference between light propagation in the atmosphere and in natural waters is wavelength dependent attenuation.

Additionally, absorption in the atmosphere is generally negligible [22], but in the ocean its magnitude can be comparable to, and sometimes larger than scattering [28]. In fact, the wavelength dependency of attenuation in the ocean almost entirely comes from absorption (Fig. 1c). The ratio of scattering to attenuation coefficients affect the backscattered signal, which is the main cause of degradation in underwater images [35, 37]. Thus, whether the water body is absorption dominated or scattering dominated must be taken into account when modeling or estimating relevant color correction parameters.

These differences suggest that strong wavelength dependent attenuation may render the atmosphere-derived image formation model inadequate when applied to underwater scenes. Indeed we recently showed [1] that the direct signal obtained from the current underwater imaging model yields wideband attenuation coefficients (the projection of the physical attenuation coefficient onto the RGB domain) that depend not only on inherent properties of the water body, but also on the camera sensor, scene radiance, and imaging range. In most works, these dependencies are not taken into consideration. For example, in [5, 12, 27] wideband attenuation coefficients were estimated by picking values at single wavelengths from physical attenuation curves (like those in Fig. 1b), ignoring the sensor response of the camera used for imaging, and all the other dependencies we showed. In one case a sum on the discrete bands of the sensor response was used but only with one water type [26]. In [6, 7] the full wavelength-dependent model was used to model underwater photographs, but was not used for image correction.

Here, we expand our work in [1] and show that the current underwater image formation model actually introduces more dependencies that were ignored until now. Specifically, we show that the wideband coefficient for backscatter strongly depends on the veiling light (i.e., time of day and water depth), and whether the water body is absorption or scattering dominated. Most importantly, we show that the wideband attenuation coefficients for the direct signal and the backscattered signal are different, despite the

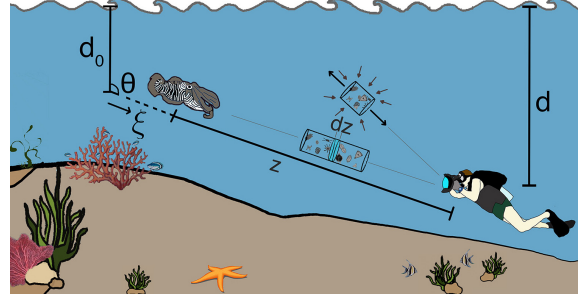


Figure 2. Ambient light attenuates exponentially with depth d reaching an object (here a giant cuttlefish), and attenuates further between the object and the sensor along the direction ξ , for a distance of z . This signal is further degraded by light scattered by particles from all directions towards the sensor.

fact that the current model assumes them to be the same. Through real-world experiments, we demonstrate the need for revising the image formation model. We perform an extensive error analysis comparing the current model to the revised one, and suggest how relevant coefficients can best be picked when all inputs to the revised model are not available. Our findings can explain the difficulties encountered thus far with image correction using the current model.

2. Light Transport in Scattering Media

2.1. Brief Oceanographic Background

In the ocean, inherent and apparent optical properties (IOPs and AOPs) govern light propagation (see Table 1 for variables and abbreviations used throughout the paper). The IOPs are only a function of the water constituents. These are *beam absorption* $a(\lambda)$, *beam scattering* $b(\lambda)$, and *beam attenuation* $\beta(\lambda)$ coefficients, where $a(\lambda)+b(\lambda)=\beta(\lambda)$. The AOPs depend on external factors such as the ambient light field [28], but are easier to measure than IOPs. Here the only AOP we use is $K_d(\lambda)$, the *diffuse attenuation coefficient of the downwelling light*, which is the extinction experienced by light penetrating a water column vertically. The magnitude of K_d only weakly depends on ambient light, so it has been used to characterize the optical qualities of water bodies, such as Jerlov's water types [21] (Fig. 1b,c).

Since both β and K_d are attenuation coefficients, which do we use in underwater computer vision? The answer is *both*, and their difference is important. While β governs the radiant power lost from a collimated beam of photons, K_d is defined in terms of the decrease of the ambient downwelling irradiance with depth, due to all photons heading in the downward direction in a diffuse (or, uncollimated) manner [28]. Generally, β is 2-5 times greater than K_d [23], and both contribute to the effective attenuation captured in a photograph, as we discuss in the next section.

Variable	Description
λ	wavelength
$a(\lambda)$	beam absorption coefficient
$b(\lambda)$	beam scattering coefficient
$\beta(\lambda)$	beam attenuation coefficient: $a(\lambda) + b(\lambda)$
$K_d(\lambda)$	diffuse downwelling attenuation coefficient
$E(z, \lambda)$	irradiance
$L(z, \lambda)$	radiance
Y	luminance
$S_c(\lambda)$	sensor spectral response
$\rho(\lambda)$	reflectance
$B^\infty(\lambda)$	veiling light
c	color channels R,G,B
β_c	wideband attenuation coefficient
B_c^∞	wideband veiling light
I_c	RGB image with attenuated signal
J_c	RGB image with unattenuated signal
d	depth (vertical range)
z	range along LOS
ξ	direction in 3-space
B	backscattered light
D	direct transmitted light
F	forward scattered light
AOP	apparent optical properties
IOP	inherent optical properties
LOS	line of sight
RTE	radiance transfer equation
VSF	volume scattering function

Table 1. Variables and abbreviations used in the paper.

2.2. The Radiance Transfer Equation

In Fig. 2, we are interested in quantifying the radiance leaving the skin of the cuttlefish and reaching the point where the diver hovers. This scenario, and light propagation in other scattering media (such as air) is governed by the *radiance transfer equation* (RTE) [10], which accounts for the time-dependent, three-dimensional behavior of radiance. In its simpler and more compact classical canonical form, the RTE for a homogeneous, source free water body (i.e. no inelastic scattering or emission) is given by [28, 33]:

$$L(d; \xi; \lambda) = L_0(d_0; \xi; \lambda) e^{-\beta(\lambda)z} + \frac{L_*(d; \xi; \lambda) e^{-K_d(\lambda)z \cos \theta}}{\beta(\lambda) - K_d(\lambda) \cos \theta} \left[1 - e^{-[\beta(\lambda) - K_d(\lambda) \cos \theta]z} \right], \quad (1)$$

where $L_0(d_0; \xi; \lambda)$ is the total radiance leaving the object; $L(d; \xi; \lambda)$ is the total radiance reaching the diver; ξ is a direction in 3D space, λ is wavelength, θ is the angle measured from nadir direction (positive looking down as conventional in oceanography), and z is the geometric distance along ξ . L_* is the path function describing radiance gained along the direction ξ from photons arriving from all directions [28].

When viewing direction is horizontal ($\theta = 90^\circ; d = d_0$), Eq. 1 becomes a function of only one attenuation coefficient (β) and simplifies to:

$$L(d_0; \xi; \lambda) = L_0(d_0; \xi; \lambda) e^{-\beta(\lambda)z} + \frac{L_*(d; \xi; \lambda)}{\beta(\lambda)} (1 - e^{-\beta(\lambda)z}) \quad (2)$$

When $\theta \neq 90^\circ$, however, we are reminded of one of the reasons why color reconstruction of underwater images is challenging: depending on the viewing angle θ , the magnitude of effective attenuation coefficient in a given scene changes! It can range from $[\beta(\lambda) - K_d(\lambda)]$ when looking up, improving visibility, to $[\beta(\lambda) + K_d(\lambda)]$ when looking down, significantly reducing it.

The first term in both Eqs. 1 & 2 is the *object radiance* resulting from photons traveling directly from the object to the observer, and the second term is the *path radiance*, which accounts for the photons reaching the observer from all directions. From here on, we will refer to them as D for *direct signal*, and B for *backscattered signal*. Then, Eq. 1 can be written as:

$$L = D + B. \quad (3)$$

Note that in Eq. 1, we omitted the in-scattering term (also called forward scattering, F). This term would have represented the light that was reflected from the object *away* from the line of sight (LOS), but through re-scattering, got realigned at small angles along the LOS. Authors in [35] showed quantitatively that $F \ll D$, and it does not contribute significantly to the degradation of an image.

2.3. Backscattered Signal, B

We investigated the direct signal in Eq. 1 in [1]. Here, we focus on *backscatter* [35], also called *path radiance* [33].

Particles in the medium scatter the light incident on them in many other directions, acting as sources of light. Backscatter is the signal formed by these photons reaching the observer carrying no information regarding the scene that is being viewed. In Eq. 1, the path radiance L_* is the radiance gained along a direction ξ owing to scattering into that direction from photons traveling in all other directions ξ' [28]. The probability of a photon traveling in a given direction after hitting a particle is determined by the *volume scattering function* (VSF). The VSF (a fundamental IOP from which all other scattering coefficients are derived), changes based on the type and concentration of particulate matter in the water body, is difficult to measure, and has only generally been quantified for a clear lake and a turbid coastal harbor [28]. The integral of the VSF across all directions yields the total scattering coefficient $b(\lambda)$, which is the main parameter governing backscatter [17, 30, 35, 41], and is readily available for Jerlov's water types [38].

Consider again an infinitesimally small disk of thickness dz , that is not on the LOS (upper disk in Fig. 2). The ra-

diance dL scattered from this disk in all directions is given by [17, 20, 28, 33]:

$$dL(z, \lambda) = b(\lambda)E(d, \lambda)dz , \quad (4)$$

where $E(d, \lambda)$ is ambient light at depth d , which is also the radiance incident on the disk in this case. Along the LOS, at a distance z away, the received radiance based on Beer's Law of exponential decay becomes [1, 28, 33]:

$$dB(z, \lambda) = dL(z, \lambda)e^{-\beta(\lambda)z} . \quad (5)$$

Substituting Eq. 4 in Eq. 5 and integrating with respect to z from $z_1 = 0$ to $z_2 = z$ gives us the backscattered signal as a function of wavelength λ :

$$B(z, \lambda) = \frac{b(\lambda)E(d, \lambda)}{\beta(\lambda)} \left(1 - e^{-\beta(\lambda)z}\right) . \quad (6)$$

When z is selected to be large enough, we can obtain the value of backscatter at infinity, also termed *veiling light*. Thus as $z \rightarrow \infty$:

$$B^\infty(\lambda) = \frac{b(\lambda)E(d, \lambda)}{\beta(\lambda)} . \quad (7)$$

Then, the total signal T at the observer is:

$$T = E(d, \lambda)e^{-\beta(\lambda)z} + B^\infty(\lambda)(1 - e^{-\beta(\lambda)z}) . \quad (8)$$

2.4. Working in Camera Space

Now, we assume the observer has a camera with spectral response $S_c(\lambda)$ where $c = R, G, B$ represents color channels. The signal in Eq. 8 is integrated to obtain the intensity of the image formed at the sensor at a horizontal distance z away from the object:

$$I_c = \frac{1}{\kappa} \int_{\lambda_1}^{\lambda_2} S_c(\lambda)\rho(\lambda)E(d, \lambda)e^{-\beta(\lambda)z}d\lambda + \frac{1}{\kappa} \int_{\lambda_1}^{\lambda_2} S_c(\lambda)B^\infty(\lambda)(1 - e^{-\beta(\lambda)z})d\lambda , \quad (9)$$

where $\rho(\lambda)$ is the reflectance spectrum of the object, κ is a scalar governing image exposure and camera pixel geometry [19], and λ_1 and λ_2 define the bounds of integration over the electromagnetic spectrum.

At depth d , the unattenuated image J_c is:

$$J_c = \frac{1}{\kappa} \int_{\lambda_1}^{\lambda_2} S_c(\lambda)\rho(\lambda)E(d, \lambda)d\lambda . \quad (10)$$

The veiling light B_c^∞ as captured by the same sensor is:

$$B_c^\infty = \frac{1}{\kappa} \int_{\lambda_1}^{\lambda_2} S_c(\lambda) \frac{b_c E_c}{\beta_c} d\lambda . \quad (11)$$

2.5. The Current Underwater Imaging Model

The current underwater imaging model for ambient illumination assumes camera response to be delta functions ($S_c(\lambda) = S_c\delta(\lambda)$), or alternatively, attenuation to vary negligibly with wavelength. Accordingly, Eq. 9 is simplified to [4, 8, 12, 17, 26, 30, 35]:

$$I_c = J_c \cdot e^{-\beta_c z} + B_c^\infty \cdot (1 - e^{-\beta_c z}) , \quad (12)$$

similarly to the atmospheric dehazing equation. Here β_c are the wideband (R, G, B) attenuation coefficients.

3. The Need for a Revised Model

3.1. Dependencies of Attenuation Coefficients

We showed in [1] that the wideband attenuation coefficients β_c estimated from the direct signal approximated by Eq. 12 have implicit dependencies on sensor response $S_c(\lambda)$, imaging range z , scene reflectance $\rho(\lambda)$, and irradiance $E(\lambda)$. From this point on, we label this coefficient β_c^D to indicate that it has been derived from the direct transmission (D) term. From Eq. 12, it is given as [1]:

$$\beta_c^D = \ln \left[\frac{D_c(z)}{D_c(z + \Delta z)} \right] / \Delta z . \quad (13)$$

Evaluating the first term in Eq. 10 with $z_1 = z$, and $z_2 = z + \Delta z$, we obtain [1]:

$$\beta_c^D = \ln \left[\frac{\int_{\lambda_1}^{\lambda_2} S_c(\lambda)\rho(\lambda)E(\lambda)e^{-\beta(\lambda)z}d\lambda}{\int_{\lambda_1}^{\lambda_2} S_c(\lambda)\rho(\lambda)E(\lambda)e^{-\beta(\lambda)(z+\Delta z)}d\lambda} \right] / \Delta z . \quad (14)$$

Now we examine the backscattered signal. Following Eq. 9, the backscatter at the sensor at a distance z is:

$$B_c = \frac{1}{\kappa} \int_{\lambda_1}^{\lambda_2} S_c(\lambda)B^\infty(\lambda) \left(1 - e^{-\beta(\lambda)z}\right) d\lambda , \quad (15)$$

We equate this exact equation to the backscatter term of the current underwater imaging model given by Eq. 12:

$$B_c(z) = B_c^\infty(1 - e^{-\beta_c z}) . \quad (16)$$

Thus, the wideband backscatter coefficient from Eq. 12 is:

$$\beta_c^B = -\ln \left(1 - \frac{B_c(z)}{B_c^\infty}\right) / z , \quad (17)$$

Substituting Eq. 15 into Eq. 17 yields

$$\beta_c^B = -\ln \left(1 - \frac{\int_{\lambda_1}^{\lambda_2} S_c(\lambda)B^\infty(\lambda)(1 - e^{-\beta(\lambda)z})d\lambda}{\int_{\lambda_1}^{\lambda_2} B^\infty(\lambda)S_c(\lambda)d\lambda}\right) / z . \quad (18)$$

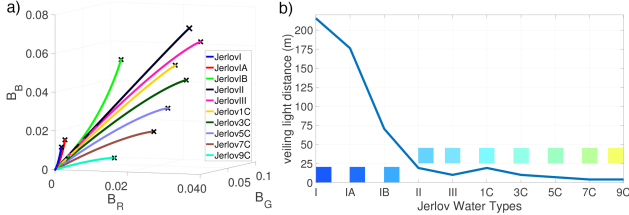


Figure 3. **a)** Physically valid space of backscatter B_c (Eq. 15) for a Nikon D90. Black x's denote the veiling light B_c^∞ for a given water type. **b)** Veiling light distance (when backscatter is saturated), varies an order of magnitude across absorption dominated (I-IB) versus scattering dominated water types (II, III, 1-9C). Colored patches are RGB renderings of the expected hue at 2m depth when backscatter is saturated. Water properties are used from [38].

We can see that β_c^B depends on the sensor response $S_c(\lambda)$, range z , and the veiling light B_c^∞ , which depends on the scattering and attenuation coefficients $b(\lambda)$ and $\beta(\lambda)$, and ambient light $E(\lambda)$ (Eq. 11). Comparing Eq. 17 with the direct signal effective attenuation

$$\beta_c^D = -\ln \left(\frac{I_c(z) - B_c(z)}{J_c} \right) / z , \quad (19)$$

reveals that the effective wideband coefficients β_c from the two terms of Eq. 12 are theoretically different although they are currently treated the same.

3.2. Physically Valid Space of β_c^B

Next, we derive the physically valid space of β_c^B analogous to that of β_c^D in [1]. We use the spectral response of a Nikon D90 and assume CIE D65 at the surface. We use Eq. 15 to calculate B_c , and Eq. 17 to extract β_c^B for z values ranging from 1m to the veiling light distance (i.e. when backscatter saturates). Values of $b(\lambda)$ were taken from [38]. Fig. 3a shows B_c for each water type at 2m depth, where each 'x' denotes the veiling light B_c^∞ calculated using Eq. 11. Note that the distance at which veiling light is reached can range from 10s to 100s of meters depending on the attenuation coefficient of the water (Fig. 3b).

Fig. 4a shows that β_c^B changes very little with z for a given water type (filled circles). This allows us to use the mean β_c^B value as a representation of each water type. We fit two lines to these β_c^B means in 3-space: one for clear water where attenuation is dominated by absorption (Fig. 1c; I-IB), and one for water types where scattering is more dominant (Fig. 1c; II, III, 1-9C). These lines denote the locus of β_c^B in 3-space (Fig. 4b).

The magnitude of veiling light B_c^∞ is directly proportional to the ambient light (i.e., depth), which in turn, causes the locus of β_c^B to move (Fig. 4c,d). Finally, we note that while the locus of β_c^D was shown to depend on camera sensor response, that of β_c^B is less sensitive to it. This is likely because the backscattered signal is formed independent of

the reflectance of objects in a scene, and depends, most strongly, on ambient light, which attenuates rapidly with depth. Fig. 4e shows the β_c^B locus for 74 cameras (Arriflex, Canon, Casio, Fuji, Hasselblad, Kodak, Leica, Manta, Nikon, Nokia, Olympus, Panasonic, Pentax, Phase One, Point Gray, Sony, Sigma) for absorption-dominated water types; camera details and loci for scattering-dominated water types are given in Supplementary Material.

3.3. β_c^D Vs. β_c^B

Fig. 4f&g compare β_c^D and β_c^B for the same scene in the same water. We simulated a diver at 5m, photographing two Macbeth charts placed horizontally at 1&10m from him. We calculated the RGB values of these charts using Eq. 9 with the response of a Nikon D90, assuming CIE D65 at the surface for clear oceanic water (Jerlov I, Fig. 4f), and a murky coastal harbor (Jerlov III, Fig. 4g). Then, using Eqs. 17&19, we extracted the wideband attenuation coefficients. As we showed in [1], β_c^D depends on reflectance, and ends up having a different value for each patch of the Macbeth chart (colored squares). The value of β_c^D also depends on the distance between the camera and the charts, so the charts cluster in different parts of the β_c space. In contrast, there is one β_c^B value per scene (black x's), and it varies very little by distance. Yet, the value of β_c^B for both water types is different than the β_c^D values for both charts.

4. A Revised Image Formation Model

In light of our findings in Secs. 3.1 & 3.2, we propose the following revised underwater image formation model:

$$I_c = J_c e^{-\beta_c^D(\mathbf{v}_D) \cdot z} + B_c^\infty \left(1 - e^{-\beta_c^B(\mathbf{v}_B) \cdot z} \right) . \quad (20)$$

Here, the vectors \mathbf{v}_D and \mathbf{v}_B represent the coefficient dependencies $\mathbf{v}_D = \{z, \rho, E, S_c, \beta\}$ and $\mathbf{v}_B = \{E, S_c, b, \beta\}$. To parallel Eq. 12, we also only considered the horizontal imaging case, but extension to other directions as given in Eq. 1 is straightforward.

5. Validation Via Real-world Experiments

5.1. Backscatter Estimation From Photographs

The image signal I_c in Eq. 9 is exactly equal to backscatter B_c for a perfect black object ($\rho = 0$). While efforts have been made to manufacture a surface close to a perfect black [18], these materials are not commercially available in small quantities. Thus, we used a color chart and leveraged the fact that the gray patches reflect light uniformly at different percentages in a linear image [2]. We fit a line to the RGB intensities corresponding to each patch using their known luminances (chromaticity coordinate Y). The value of this line at $Y = 0$, which would have been the luminance of perfect black (Fig. 5a), is the B_c for that color channel.

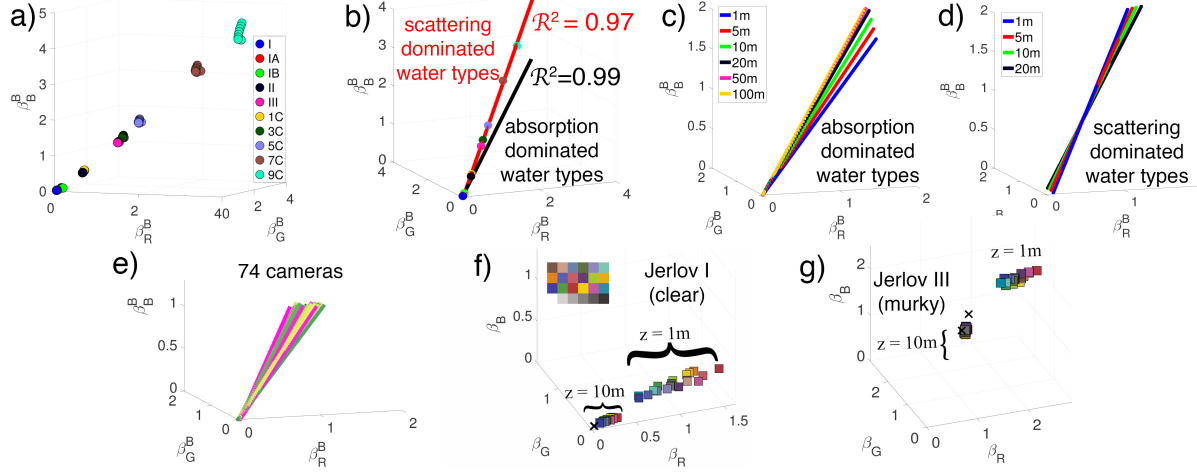


Figure 4. Physically valid space of β_c^B . **a)** We calculated β_c^B at a vertical depth of 1m, for horizontal distances from 1m up to the veiling light distance. The resulting β_c^B varied only slightly with horizontal distance. **b)** We averaged the β_c^B for all horizontal distances within each water type, and fit two lines in 3-space that describe its locus in absorption (black) and scattering (red) dominated water types. The coefficient of determination, R^2 , shows an excellent linear fit for both. **c & d)**: The locus of β_c^B is sensitive to ambient light, which affects $B^\infty(\lambda)$. Lines are plotted according to vertical depth, which attenuates the ambient illumination. **e)** For most common cameras the locus of β_c^B is weakly sensitive to sensor response. Here we show the locus for 74 cameras, for absorption dominated water types only, at 10 m depth, and D65 as surface light. See Supplementary Material for camera details and other water types. **f)** The behavior of β_c^B (black x's) vs. β_c^D (colored squares) in clear and **g)** murky water. As predicted by Eqs. 14 & 18, β_c^B and β_c^D are different. Moreover, there is a single β_c^B value for the entire scene, but a β_c^D value for every color (and distance) in the scene.

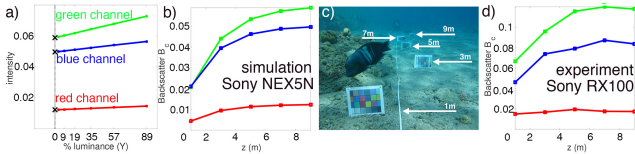


Figure 5. **a)** Calculating B_c from gray patches, here $Y = 3, 9, 30, 35, 58, 90\%$ for Macbeth chart. The ordinates of each line (X's) denote backscatter. **b)** Simulation of the expected behavior of B_c based on Eq. 8. **c)** Underwater experiment validating the backscatter estimation method in Sec. 5.1. **d)** B_c extracted for each chart in **c**), showing the expected exponential increase with distance.

Fig. 5b shows B_c simulated in water type II (equally dominated by absorption and scattering) using Eq. 9, along a horizontal transect of 10m, at a depth of 2m. We used the response of a Sony NEX5N and assumed surface light was CIE D65. Fig. 5c&d show the validation of this method in the coastal part of the Red Sea (type IB or II [1]). For this experiment, we used a Sony RX100. Due to the differences in sensor response and ambient conditions, magnitudes in Fig. 5b&d are not directly comparable, but both convey the expected exponential behavior of B_c with z .

5.2. Validation of β_c^B locus

We conducted underwater experiments in the Red Sea and the Mediterranean (Fig. 6). For each experiment, we laid out 5 colors charts at horizontal distances of 1,3,5,7

and 9m from the camera. In the Red Sea, we tested a Nikon D810 and a Sony RX100 simultaneously (Fig. 6a), taking 5–10 photographs of scenes at 2&6m depth. In the Mediterranean, we photographed scenes at 6&10m only with a Nikon D810. All images were taken in raw format, in manual mode, keeping the settings consistent for each camera for a given scene.

From each photo, we calculated B_c as described in Sec. 5.1, and extracted β_c^B using Eq. 17. We did not have the Nikon D810 response, so used the mean response of all Nikons from Fig. 4e to draw the loci in Fig. 6b, and used CIE D65 for surface light. The loci for the Red Sea 2&6m scenes (Fig. 6b) were different as predicted. The β_c^B extracted from both Nikon (green dots) and Sony photos (red dots) aligned closely with the ‘mean Nikon’ locus; each dot represents the average coefficient ($\beta_c^B_{2m} = [0.32, 0.22, 0.18]$ for 2m, and $\beta_c^B_{6m} = [0.29, 0.25, 0.2]$) of five color charts in each photo.

The locus of β_c^D is expected to move based on sensor [1]. We did not have Sony RX100 response, so in Fig. 6c we show β_c^D locus for ‘mean Nikon’, for water type II, for distances varying from 1–9m (matching our experiments). Each filled circle represents β_c^D for a given color patch at a given distance in the scene. As with β_c^B , experimental data validate the expected locus of β_c^D , and as predicted, β_c^B and β_c^D do not have the same values.

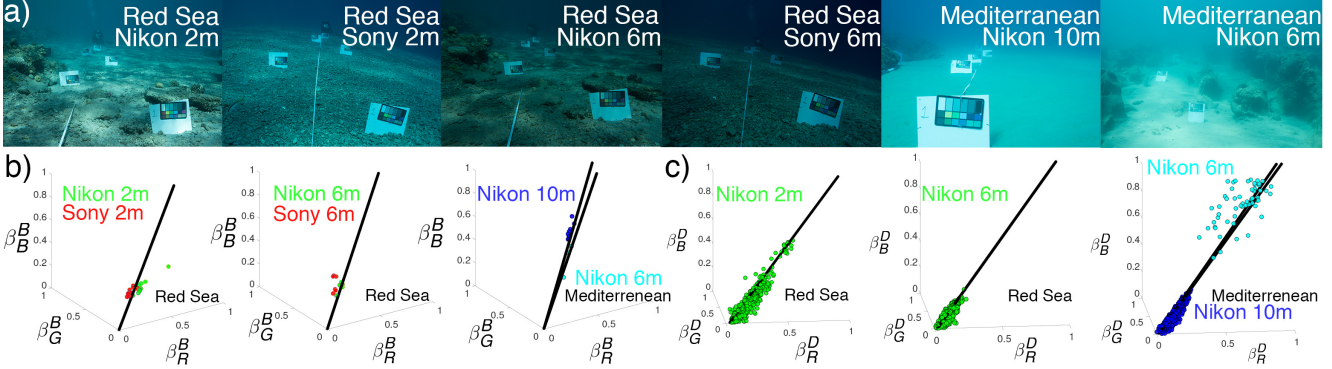


Figure 6. Real-world experiments in the Red Sea and the Mediterranean. **a)** We laid out 5 DGK waterproof color charts at depths of 2, 6, and 10m at horizontal distances of 1,3,5,7 and 9m from the camera. In the Red Sea, we used a Nikon D810 and a Sony RX100 simultaneously. In the the Mediterranean, we only used the Nikon D810. In all cases loci were drawn for type II, according to the ‘mean Nikon’ response of cameras in Fig. 4e. **b)** Estimated β_c^B . As our simulations predicted, β_c^B varies more strongly with water type and depth, than with sensor response, and coefficients from both cameras fall on the locus. **c)** Estimated β_c^D . As with β_c^B , the coefficients extracted from underwater experiments fall closely on the predicted locus. More importantly, despite the fact that the current imaging model treats them to be the same, β_c^B and β_c^D are different.

6. Error Analysis: Current Vs. Revised Model

While the model in Eq. 20 is the most accurate, we realize it is difficult to obtain all its parameters given their dependencies. Therefore, we performed an extensive error analysis to quantify the effect of every part in the revised model. We tested seven scenarios of color reconstruction using the current (Eq. 12) and revised (Eq. 20) models with different parameters:

- S1.** Current model with $\beta_c = \beta_c^B$.
- S2.** Current model with β_c derived from the chart at $z = 1\text{m}$ (i.e., $\beta_c = \beta_c^D(z = 1\text{m})$).
- S3.** Current model with $\beta_c = \beta_c^D(z = 5\text{m})$.
- S4.** Revised model with the correct β_c^B and $\beta_c^D(z = 1\text{m})$.
- S5.** Revised model with the correct β_c^B and $\beta_c^D(z = 5\text{m})$.
- S6.** Revised model with the correct β_c^B and $\beta_c^D(z)$, where $\beta_c^D(z)$ is obtained from the average of $\beta_c^D(z, \rho)$ values for all color patches for each chart at a given z .
- S7.** Revised model with the correct β_c^B and $\beta_c^D(z, \rho)$, where $\beta_c^D(z, \rho)$ is the coefficient calculated for each color patch at each range.

We synthesized a scene using Eq. 9 where a diver at 2m depth is photographing 5 color charts horizontally in front of him at $z = 1, 3, 5, 7, 9\text{m}$. For all simulations we used b and β of Jerlov II, S_c of a Nikon D90, took $E(0, \lambda)$ to be CIE D65, and the reflectances ρ of a Macbeth chart. The ground truth β_c corresponding to this simulation are shown in Fig. 7a. Error between the unattenuated color J (Eq. 10) and the reconstructed one \hat{J} (found either inverting Eq. 12 or 20) is measured as the dissimilarity α between them in RGB space (Fig. 7b):

$$\cos \alpha = J \cdot \hat{J} / (|J| \cdot |\hat{J}|) . \quad (21)$$

6.1. Corrections Using The Current Model

For all patches, errors resulting from using the current image formation model using only β_c^B are consistent across range z (**S1**, black curves in Fig. 7b), except for colored patches where they slightly increase with z . In contrast, using the current model with β_c^D extracted from only one of the charts at $z = 1\text{m}$, averaged for all colors, yields errors that are small for $z = 1\text{m}$ but significantly increase with z (**S2**). This is because the magnitude of $\beta_c^D(z = 1\text{m})$ is larger than β_c^D at other z , and it also yields an incorrect backscatter calculation. However when the same correction is carried out using only $\beta_c^D(z = 5\text{m})$ (**S3**), the overall errors are reduced. This is because $\beta_c^D(z = 5\text{m})$ for every color channel is much closer to the mean β_c^D in the scene, and also closer in magnitude to β_c^B , resulting in an acceptable backscatter removal. Thus, when using the current model errors are reduced when calibration of coefficients takes places not at proximity to the camera. Thus, if one is only able to estimate a single β_c^D value, choosing coefficients from a mean z might prevent extremely high or low values in the corrected image. Note that this suggests that estimating coefficients from color charts that are close to the camera, as is often done, is a bad habit. Yet, **S3** still yields visible errors in the hues of the reconstructed colors, especially for large z .

6.2. Corrections Using The Revised Model

If backscatter is removed using the correct β_c^B , but the colors are reconstructed using the β_c^D extracted only from the first chart (**S4**), errors remain almost identical to **S2**, implying that β_c^D has a more prominent role in color reconstruction than β_c^B . The only noticeable improvement is in the reconstruction of black, but the errors still increase with

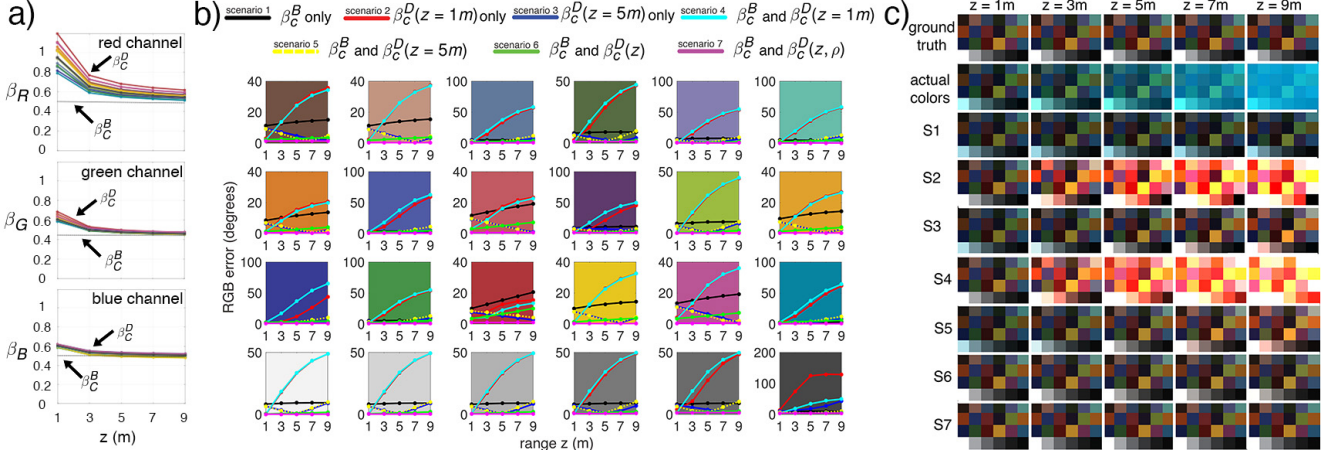


Figure 7. a) Ground truth values for β_c^B (dashed line) and β_c^D (lines colored according to the 24 patches). The value of β_c^B almost does not change with z , while β_c^D decreases logarithmically. b) Color reconstruction error for the seven cases listed in Sec. 6 using Eq. 21, and c) RGB visualization of errors. Each chart is white balanced using the white patch of the ground truth image.

z , likely due to the overcompensation from β_c^D calculated at $z = 1\text{m}$. The overcompensation due to β_c^D calculated at distances close to the camera is relevant for all water types (see Supplementary Material).

In **S5**, we extract β_c^D from the middle chart placed at $z = 5\text{m}$ (yellow curves in Fig. 7b). This causes a drop in error when compared to **S4** because as Fig. 7a shows, β_c^D decreases logarithmically with increasing distance in a scene. Thus, $\beta_c^D(z = 1\text{m})$ greatly overcompensates the colors in the rest of the scene, whereas $\beta_c^D(z = 5\text{m})$ is close to the average β_c^D in the entire scene.

When β_c^D is expressed as a function of z , the error magnitudes decrease significantly (**S6**). In this case, we calculated one β_c^D value calculated per chart (i.e., at the z corresponding to each chart), which is averaged over all reflectances ρ . For this scenario, the highest errors arise for the colors that contain red. This is because for those colors when $z > 5\text{m}$ the magnitude of $\beta_c^D(z)$ becomes less than that of $\beta_c^D(z = 5\text{m})$, and $\beta_c^D(z = 5\text{m})$ estimates the corresponding coefficient better. In contrast, for colors containing blue, when $z > 5\text{m}$, the opposite happens: $\beta_c^D(z)$ value becomes closer to the corresponding coefficients and the errors decrease when compared to **S5**. Yet, even with the higher errors associated with colors containing red, errors resulting from **S6** are almost as low as errors resulting from **S7** - a nearly perfect reconstruction using $\beta_c^D(z, \rho)$ (magenta curves in Fig. 7b).

In real life, having β_c^D for every z and ρ for a scene is difficult, but can be done, for example, using structure-from-motion to group patches corresponding to the same objects at different known distances [8]. Then our loci calculation and simulation might be used to estimate the β_c^D value per distance per object. Even if this scheme is not possible, our insights demonstrate the importance of choosing the best

distance to estimate β_c^D from.

7. Discussion

We demonstrated through theoretical analysis and real-world experiments that the commonly used underwater image formation model yields errors that were not accounted for thus far. We showed that the coefficient associated with backscatter varies with sensor, ambient illumination, and water type; and most importantly, it is different than the coefficient associated with the direct signal. These, together with dependencies we showed in [1], might explain many inaccuracies and instabilities in current algorithms. Our revised model will lead to the development of methods that will better correct complex underwater scenes.

Acknowledgements

This work was supported by the The Leona M. and Harry B. Helmsley Charitable Trust, the Maurice Hatter Foundation, and Ministry of Science, Technology and Space grant #3 – 12487, the Technion Ollendorff Minerva Center for Vision and Image Sciences, the University of Haifa institutional postdoctoral program. We thank Tom Shlesinger, Deborah Levy and Matan Yuval for help with experiments, and the Interuniversity Institute of Marine Sciences in Eilat for logistical support. Additionally, we thank Ella Treibitz for the invaluable support we received from her during various phases of this manuscript.

References

- [1] D. Akkaynak, T. Treibitz, T. Shlesinger, R. Tamir, Y. Loya, and D. Iluz. What is the space of attenuation coefficients in underwater computer vision? In *Proc. IEEE CVPR*, 2017. 2, 3, 4, 5, 6, 8

- [2] D. Akkaynak, T. Treibitz, B. Xiao, U. A. Gürkan, J. J. Allen, U. Demirci, and R. T. Hanlon. Use of commercial off-the-shelf digital cameras for scientific data acquisition and scene-specific color calibration. *JOSA A*, 31(2):312–321, 2014. 5
- [3] Y. Bahat and M. Irani. Blind dehazing using internal patch recurrence. In *Proc. IEEE ICCP*, 2016. 1
- [4] D. Berman, T. Treibitz, and S. Avidan. Non-local image dehazing. In *Proc. IEEE CVPR*, 2016. 1, 4
- [5] D. Berman, T. Treibitz, and S. Avidan. Diving into haze-lines: Color restoration of underwater images. In *Proc. British Machine Vision Conference (BMVC)*, 2017. 1, 2
- [6] H. Blasinski and J. Farrell. A three parameter underwater image formation model. *Electronic Imaging*, 2016(18):1–8, 2016. 2
- [7] H. Blasinski and J. E. Farrell. Simulation of underwater imaging systems. In *Imaging Systems and Applications*, pages IT3A–3. Optical Society of America, 2015. 2
- [8] M. Bryson, M. Johnson-Roberson, O. Pizarro, and S. B. Williams. True color correction of autonomous underwater vehicle imagery. *J. of Field Robotics*, 2015. 1, 4, 8
- [9] N. Carlevaris-Bianco, A. Mohan, and R. M. Eustice. Initial results in underwater single image dehazing. In *Proc. IEEE/MTS Oceans*, 2010. 1
- [10] S. Chandrasekhar. *Radiative transfer*. Courier Corporation, 2013. 3
- [11] C. C. Chen. Attenuation of electromagnetic radiation by haze, fog, clouds, and rain. Technical report, RAND CORP SANTA MONICA CA, 1975. 1
- [12] J. Y. Chiang and Y.-C. Chen. Underwater image enhancement by wavelength compensation and dehazing. *IEEE Trans. Image Processing*, 21(4):1756–1769, 2012. 1, 2, 4
- [13] P. Drews, E. Nascimento, F. Moraes, S. Botelho, and M. Campos. Transmission estimation in underwater single images. In *Proc. IEEE ICCV Underwater Vision Workshop*, pages 825–830, 2013. 1
- [14] R. Fattal. Dehazing using color-lines. *ACM Trans. on Graphics (TOG)*, 34(1):13, 2014. 1
- [15] M. P. Gall, R. J. Davies-Colley, and R. A. Merrilees. Exceptional visual clarity and optical purity in a sub-alpine lake. *Limnology and Oceanography*, 58(2):443–451, 2013. 2
- [16] U. T. Hammer. *Saline lake ecosystems of the world*, volume 59. Springer Science & Business Media, 1986. 2
- [17] K. He, J. Sun, and X. Tang. Single image haze removal using dark channel prior. *Trans. IEEE PAMI*, 33(12):2341–2353, 2011. 1, 2, 3, 4
- [18] M. K. Hedayati, M. Javaherirahim, B. Mozooni, R. Abdellaziz, A. Tavassolizadeh, V. S. K. Chakravadhanula, V. Zaporjchenko, T. Strunkus, F. Faupel, and M. Elbahri. Design of a perfect black absorber at visible frequencies using plasmonic metamaterials. *Advanced Materials*, 23(45):5410–5414, 2011. 5
- [19] C. P. Huynh and A. Robles-Kelly. Comparative colorimetric simulation and evaluation of digital cameras using spectroscopy data. In *Digital Image Computing Techniques and Applications, 9th Biennial Conference of the Australian Pattern Recognition Society on*, pages 309–316. IEEE, 2007. 4
- [20] J. S. Jaffe. Computer modeling and the design of optimal underwater imaging systems. *IEEE J. Oceanic Eng.*, 15(2):101–111, 1990. 4
- [21] N. Jerlov. *Irradiance Optical Classification*. Elsevier, 1968. 1, 2
- [22] A. Kokhanovsky. Optical properties of terrestrial clouds. *Earth-Science Reviews*, 64(3):189–241, 2004. 1, 2
- [23] Z. Lee, S. Shang, C. Hu, K. Du, A. Weidemann, W. Hou, J. Lin, and G. Lin. Secchi disk depth: A new theory and mechanistic model for underwater visibility. *Remote sensing of environment*, 169:139–149, 2015. 2
- [24] A. Levis, Y. Y. Schechner, and A. B. Davis. Multiple-scattering microphysics tomography. In *Proc. IEEE CVPR*, 2017. 1
- [25] A. Levis, Y. Y. Schechner, and R. Talmon. Statistical tomography of microscopic life. In *Proc. IEEE CVPR*, 2018. 1
- [26] H. Lu, Y. Li, S. Nakashima, and S. Serikawa. Turbidity underwater image restoration using spectral properties and light compensation. *IEICE trans. on Information and Systems*, 99(1):219–227, 2016. 1, 2, 4
- [27] H. Lu, Y. Li, L. Zhang, and S. Serikawa. Contrast enhancement for images in turbid water. *JOSA A*, 32(5):886–893, 2015. 1, 2
- [28] C. D. Mobley. *Light and water: radiative transfer in natural waters*. Academic press, 1994. 2, 3, 4
- [29] S. G. Narasimhan and S. K. Nayar. Chromatic framework for vision in bad weather. In *Proc. IEEE CVPR*, volume 1, pages 598–605. IEEE, 2000. 2
- [30] S. G. Narasimhan and S. K. Nayar. Vision and the atmosphere. *Int. J. Computer Vision*, 48(3):233–254, 2002. 2, 3, 4
- [31] Y.-T. Peng, X. Zhao, and P. C. Cosman. Single underwater image enhancement using depth estimation based on blurriness. In *Proc. IEEE ICIP*, pages 4952–4956, 2015. 1
- [32] U. Platt, K. Pfeilsticker, and M. Vollmer. *Radiation and Optics in the Atmosphere*, pages 1165–1203. Springer New York, New York, NY, 2007. 1, 2
- [33] R. Preisendorfer. Hydrologic optics. volume i. introduction. 1976 251, 1976. 3, 4
- [34] D. Rouwet, B. W. Christenson, F. Tassi, and J. Vandemeulebrouck. *Volcanic Lakes*. Springer, 2015. 2
- [35] Y. Y. Schechner and N. Karpel. Clear underwater vision. In *Proc. IEEE CVPR*, 2004. 2, 3, 4
- [36] Y. Y. Schechner and N. Karpel. Recovery of underwater visibility and structure by polarization analysis. *IEEE J. Oceanic Engineering*, 30(3):570–587, 2005. 1
- [37] M. Sheinin and Y. Y. Schechner. The next best underwater view. In *Proc. IEEE CVPR*, pages 3764–3773, 2016. 2
- [38] M. G. Solonenko and C. D. Mobley. Inherent optical properties of jerlov water types. *Applied optics*, 54(17):5392–5401, 2015. 1, 3, 5
- [39] R. Tan. Visibility in bad weather from a single image. In *Proc. IEEE CVPR*, 2008. 1
- [40] H.-Y. Yang, P.-Y. Chen, C.-C. Huang, Y.-Z. Zhuang, and Y.-H. Shiau. Low complexity underwater image enhancement based on dark channel prior. In *Proc. IEEE Int. Conf. on Innovations in Bio-inspired Computing and Applications*, pages 17–20, 2011. 1

- [41] X. Zhao, T. Jin, and S. Qu. Deriving inherent optical properties from background color and underwater image enhancement. *Ocean Engineering*, 94:163–172, 2015. 3